Research Article | Vol. 31, No. 12 / 5 Jun 2023 / Optics Express 20410

Optics EXPRESS

Fast and rigorous optical simulation of periodically corrugated light-emitting diodes based on a diffraction matrix method

CHANHYUNG PARK,[1,†] JEONGMIN SHIN,[1,†] SANMUN KIM,[1] SONGJU LEE,[1] JUHO PARK,[1] JAEHYEOK PARK,[1] SEHONG PARK,[2] SEUNGHYUP YOO,[1,3] AND MIN SEOK JANG[1,4]

[1]*School of Electrical Engineering, Korea Advanced Institute of Science and Technology, 34141 Daejeon, Republic of Korea*
[2]*OC Optical Technology Task, LG Display, 07796 Seoul, Republic of Korea*
[3]*syoo_ee@kaist.ac.kr*
[4]*jang.minseok@kaist.ac.kr*
[†]These authors contributed equally to this work

Abstract: Increasing the light extraction efficiency has been widely studied for highly efficient organic light-emitting diodes (OLEDs). Among many light-extraction approaches proposed so far, adding a corrugation layer has been considered a promising solution for its simplicity and high effectiveness. While the working principle of periodically corrugated OLEDs can be qualitatively explained by the diffraction theory, dipolar emission inside the OLED structure makes its quantitative analysis challenging, making one rely on finite-element electromagnetic simulations that could require huge computing resources. Here, we demonstrate a new simulation method, named the diffraction matrix method (DMM), that can accurately predict the optical characteristics of periodically corrugated OLEDs while achieving calculation speed that is a few orders of magnitude faster. Our method decomposes the light emitted by a dipolar emitter into plane waves with different wavevectors and tracks the diffraction behavior of waves using diffraction matrices. Calculated optical parameters show a quantitative agreement with those predicted by finite-difference time-domain (FDTD) method. Furthermore, the developed method possesses a unique advantage over the conventional approaches that it naturally evaluates the wavevector-dependent power dissipation of a dipole and is thus capable of identifying the loss channels inside OLEDs in a quantitative manner.

1. Introduction

Organic light-emitting diodes (OLEDs) are widely used in various display applications spanning from mobile displays to large-area high-end televisions and also in lighting applications. They are thinner and lighter than conventional devices and possess high color purity, making them flexible and accessible to the true black level [1–5]. The process of light emission inside an OLED can be divided into two steps: the injected charge carriers recombine through the emissive channel over the non-radiative channel, and then the light escapes from the active layer to the free space. The efficiency of the first process, the internal quantum efficiency, is close to unity [6]. However, even with considerable research efforts, the efficiency of the latter, or the light extraction efficiency (LEE), is still far from perfect and limits the overall power conversion efficiency of OLEDs.

The LEE of an OLED is constrained by the coupling to the bound modes such as substrate-confined modes, waveguide modes in the organic layers, and surface plasmon polaritons (SPPs) at the organic-metal electrode interfaces [7,8]. In a planar device, the excited bound modes can never couple back to the radiative modes due to the wavevector mismatch between the modes, but are dissipated as heat, which could also reduce the lifetime of the device. To extract energy

#489758 https://doi.org/10.1364/OE.489758
Journal © 2023 Received 16 Mar 2023; revised 10 May 2023; accepted 10 May 2023; published 1 Jun 2023

Optics EXPRESS

from these bound modes to unbound radiation, researchers have investigated various strategies, such as microlens arrays [9–11], nanoparticle-embedded scattering layers [12–14], nanoholes [15], and low-index grids [16,17]. While these methods focus on extracting substrate-confined or waveguide modes, periodic or quasi-periodic corrugations increase the efficiency by extracting SPP modes as well as the waveguide modes [18–21]. Here, the periodic corrugation works as a diffraction grating, which provides the extra crystal momentum required to match the wavevector of a bound mode to that of free waves, allowing for the extraction of the energy that would otherwise be lost as a waveguide mode and SPP modes.

Although the idea of using periodic corrugation for light extraction in OLEDs is straightforward and easy to understand qualitatively, its quantitative analysis is challenging and generally requires a large computational resource; it takes hours to days to numerically calculate LEE of a periodically corrugated device using a typical high-performance server and conventional full-wave electromagnetic simulation methods such as the finite-difference time-domain (FDTD) method or the finite element method (FEM) [22–25]. This makes device geometry optimization impractical [26]. Moreover, it is difficult to gain a quantitative understanding of how the different modes are converted inside the device using conventional optical simulation methods. Although there exist efficient methods to calculate the light emission inside planar devices based on plane wave decomposition [27] and machine learning [28,29], these methods are not directly applicable to corrugated devices.

There have been a few attempts that calculate the far-field emission patterns of corrugated LEDs based on transfer or scattering matrices [30–34]. However, these methods lack an analysis of the power dissipation through bound mode excitation and therefore cannot determine the LEE of the device, as they do not calculate the Purcell effect, which eventually represents the net energy emitted from the emitters. As a result, the calculation results cannot be quantitatively verified by comparison with other full-field simulation methods. Wiessman devised an approximate approach to treat periodically corrugated LEDs and verified the result using full-field simulations [35], but this method is based on a perturbation theory and thus only applicable to a limited set of structures such as shallow etched photonic crystals. Liu and Fan developed a rigorous coupled-wave analysis (RCWA) software package that allows for tracking the wave diffraction behavior in periodically corrugated structures [36], and there have also been more elaborate considerations on the reciprocity between a light-emitting device and a solar cell [37,38]. However, these efforts were not applied to the problem of light emission from a periodically corrugated structure.

In this work, we developed a rigorous and fast optical simulation method for periodically corrugated OLEDs. By tracking the polarization and mode conversion via diffraction inside a device, the developed method, which we call the diffraction matrix method (DMM), provides an efficient way to quantitatively analyze the light emission from both point sources and planarly layered sources in corrugated OLEDs. The validity of the DMM method is checked by comparing it with FDTD simulations, and the results show that the values predicted by the DMM method are in close agreement with those given by FDTD, yet DMM is about 10^2 to 10^4 times faster than FDTD at the same accuracy. Furthermore, it is demonstrated that the DMM allows for an analysis of the loss channels in OLEDs by obtaining the power dissipation density as a function of in-plane wavevector.

2. Methods

Before we discuss how to calculate the light extraction properties of a periodically corrugated OLED, it would be instructive to understand the light emission in a simpler version of the device, a planar OLED. A planar OLED consists of vertically stacked layers of different materials with various refractive indices. Also, the light emission from an electron-hole recombination can be treated as a dipolar emission [39]. As an example, Fig. 1(a) shows a simplified schematic of a planar OLED, whose active layers are composed of organic semiconductors and light-emitting

Optics EXPRESS

dipole is embedded inside the organic layer. For structural simplicity, we ignored the glass-substrate layer and assumed that the OLED is top-emitting so that light cannot pass through the bottom metallic layer. Here, if we consider a wave component with a certain in-plane wavevector ($k_{\parallel} = \sqrt{k_x^2 + k_y^2}$), no matter how many times reflection or transmission happens, its in-plane wavevector is conserved due to the planar symmetry of the device. Therefore, all the partial waves represented as the black arrows in Fig. 1(a) occupy a single point in the in-plane k space shown in Fig. 1(b) and do not interact with the partial waves having different in-plane wavevectors. By leveraging this property, it is possible to efficiently compute the light emission property of a dipolar emitter by decomposing the dipolar emission into a sum of plane waves and then tracking the propagation of each plane wave group defined by an in-plane wavevector using simple scalar operations [27]. This method, which was proposed by Chance, Prock, and Silbey [27], allows for a fast simulation of light emission from a planar device that is a few orders of magnitude faster than general-purpose full-wave electromagnetic simulation methods such as FDTD and FEM.

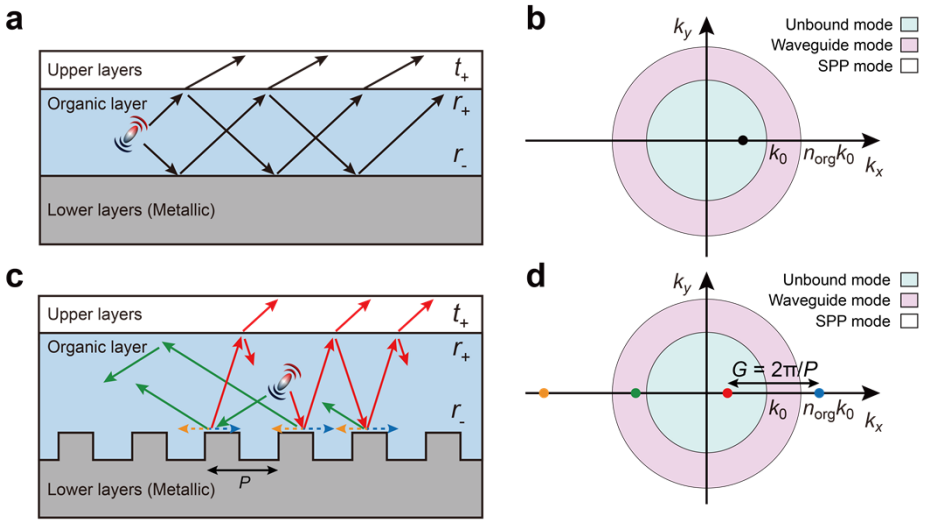

Fig. 1. Diffraction and reciprocal space of a corrugated OLED. (a) Schematic illustration of simplified ray propagation in a planar OLED**.** The arrows represent the decomposed plane waves, as well as the reflected and transmitted plane waves. **(b)** Plane waves in the organic layer of a planar OLED can be sorted into three modes: Unbound mode, waveguide mode, and SPP mode. The black arrows in **(a)** are located inside the unbound region. **(c)** Schematic illustration of simplified ray propagation in a periodically corrugated OLED. Diffraction occurs at the corrugated layer boundary, and the diffracted plane waves interfere with other plane waves (red and green arrows). Evanescent waves are also generated (yellow and blue arrows). **(d)** The plane waves in **(c)** are represented by points in reciprocal space with the same color-coding. Neighboring points are spaced by the crystal momentum which is $G = 2\pi/P$ in the reciprocal space. The plane wave that corresponds to the red point is the only one inside the unbound regime, where the power can be extracted outwards. The green arrow belongs to the waveguide mode and experiences total internal reflection at the top boundary. The yellow and blue arrow are in the SPP mode regime.

Plane wave components inside OLEDs can be roughly sorted into three modes depending on their in-plane wavevectors ($k_{\parallel}$) as depicted in Fig. 1(b). Unbound mode is a plane wave inside the light cone ($k_{\parallel} \leq k_0 = \omega/c$) that can be extracted from the device. Waveguide mode is bound mostly inside the organic layer and is defined by $k_0 < k_{\parallel} \leq n_{org}k_0$, where n_{org} is the refractive index of the organic active layer. Finally, if $k_{\parallel} > n_{org}k_0$, the mode can only exist in the form of a

Optics EXPRESS

surface bound mode at a metal-dielectric interface and is thus called surface plasmon polariton (SPP) mode [7,8]. It is important to note that, in a planar device, only the unbound mode can be extracted but the waveguide and SPP modes cannot leave the device and their energy is dissipated as heat.

Periodic corrugation has been studied as a way to extract energy from the bound modes that have been previously dissipated as heat in planar OLEDs [18]. The dynamics of light propagation inside a periodically corrugated OLED is much more complicated compared to that in a planar device. When a one-dimensional corrugation along x-direction with a period of P is present, as shown in Fig. 1(c), the in-plane wavevector of a wave is no longer conserved in x-direction but satisfies the following relation due to diffraction:

$$k_{x,m} = k_x + mG, \qquad G = \frac{2\pi}{P} \tag{1}$$

where k_x is the x-component of the incident wavevector and $k_{x,m}$ is the x-component of the m-th order diffracted wave. Figure 1(d) shows the corresponding wavevectors represented in the reciprocal space with the identical color coding as in Fig. 1(c). The distance between the neighboring two points is G as provided in Eq. (1). These plane waves form a group that is uniquely defined for a k-point in a Brillouin zone. The energy conversion due to diffraction occurs only between the plane waves belonging to the group. This implies that, as depicted in Fig. 1(c), there is a chance that the waveguide modes and the SPP modes can diffract back into the light cone and thus be extracted.

Mode conversion induced by the diffraction affects the light extraction mechanism of the device. In this work, as an extension of the transfer matrix method (TMM), we devise a diffraction matrix method (DMM), which enables the tracking of mode-conversion among the diffracted waves in a periodic structure. For simplicity, here we consider an OLED example where we have a periodic corrugation only in the bottom metallic layer and the top layers are flat as shown in Fig. 1(c). The definitions of symbols used in this article are summarized in Table 1.

The formation of diffraction matrices is visualized in Fig. 2. Unlike the case of a flat interface shown in Fig. 2(a), a periodically corrugated interface can change both the in-plane wavevector and the polarization of the incident wave by diffraction, as illustrated in Fig. 2(b). We first define an $N = 2M + 1$-dimensional vector $\mathbf{A}_{\text{in}}$ whose components are the complex amplitudes of the incident plane waves belonging to the same diffraction group (see Section S1 of Supplement 1 for detailed definition of complex amplitude (u_x)):

$$\mathbf{A}_{\text{in}} = \left[\; a_{\text{in}}(u_{x,-M}), \quad \cdots \quad a_{\text{in}}(u_{x,-1}), \quad a_{\text{in}}(u_{x,0}), \quad a_{\text{in}}(u_{x,1}), \quad \cdots \quad a_{\text{in}}(u_{x,M}) \; \right]^T \tag{2}$$

Here, M determines the number of diffraction orders used in the calculation, and $u = k/(n_{\text{org}}k_0)$ is the normalized wavevector. The reflected waves can be similarly described by using a vector $\mathbf{A}_{\text{r}}$. $\mathbf{A}_{\text{r}}$ is related to $\mathbf{A}_{\text{in}}$ by the relation $\mathbf{A}_{\text{r}} = \mathbf{R}\mathbf{A}_{\text{in}}$, where $\mathbf{R}$ is a $N \times N$ reflection matrix whose component, $r_{m,n}$, is the diffraction-resolved complex reflection coefficient for the diffraction from $u_{x,n}$ to $u_{x,m}$. For notational simplicity, we define the indices of a diffraction matrix to run from -M to M. The complex diffraction coefficients, even for the evanescent modes, are calculated using rigorous coupled-wave analysis (RCWA) with the RETICOLO RCWA package [40].

To take polarizations into account for conical diffraction, the diffraction matrices need to be extended [41]. Considering every possible combination of mode conversion between transverse magnetic (TM) and transverse electric (TE) modes, the size of $\mathbf{A}$ should be doubled with the first half accounting for TE and the second half belonging to the TM polarized waves, and the diffraction matrices should also be extended as follows (see Fig. 2(b) for a schematic representation):

$$A = \begin{bmatrix} \mathbf{A}^{\text{TE}} \\ \mathbf{A}^{\text{TM}} \end{bmatrix} \tag{3}$$

Optics EXPRESS

Table 1. Definition of symbols used in DMM

Symbol	Definition	Symbol	Definition
P	Period of corrugation	G	Crystal momentum $(2\pi/P)$
$\mathbf{k}$	Wavevector of a plane wave	n_{org}	Refractive index of the organic layer
k_0	Wavenumber of a plane wave in free space	$\mathbf{u}$	Normalized wavevector $\mathbf{k}/(n_{org}k_0)$
a $(\mathbf{u})$	Complex electric field amplitude of plane wave with a wavevector $\mathbf{u}$	$\mathbf{A}$	Diffraction group of a
M	Highest diffraction order considered in calculation	N	Total number of diffraction orders considered in calculation $(2M+1)$
$\mathbf{R}_{+,-}$	Transfer matrix describing wave reflection at the top (+) and the bottom (−) interface	$\mathbf{P}_{+,-}$	Transfer matrix describing wave propagation within the organic layer above (+) and below (−) the emission plane
$\mathbf{C}_{+,-}$	$\mathbf{P}_{+}\mathbf{P}_{-}\mathbf{R}_{+,-}$	$T_{+}(\mathbf{u})$	Transmittance at the top interface
p_0	Electric dipole moment of an emitter	F_{∞}	Net power emitted from an emitter (or emitting plane) in a bulk material with refractive index n_{org}
$K(\mathbf{u})$	Power dissipation density by an emitter (or emitting plane) through wave emission with a wavevector $\mathbf{u}$ in a device	F	Net power emitted from an emitter (or emitting plane) in a device
$K_{out}(\mathbf{u})$	Radiative power density escaping from a device through plane waves with a wavevector $\mathbf{u}$	F_{out}	Net radiative power escaping from a device
LEE	Light extraction efficiency (F_{out}/F)	η	Purcell factor (F/F_{∞})
n_{RCWA}	Number of Fourier orders considered in RCWA	n_{BZ}	Number of sampled k points in the Brillouin zone

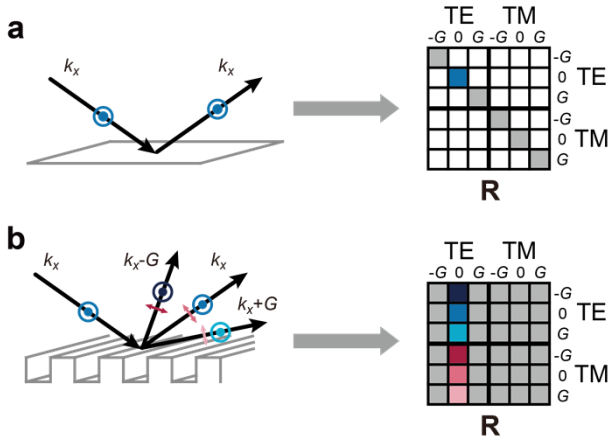

Fig. 2. The diffraction matrix formalism. Diffraction matrix formation for the planar boundary **(a)** and the periodically corrugated boundary **(b)** At the planar boundary, the magnitude of in-plane wavevector and the polarization are conserved upon reflection. Therefore, the diffraction matrix will be a diagonal matrix. However, at the periodically corrugated boundary, power is transferred to planewaves with different in-plane wavevector and polarization. Therefore, non-diagonal elements may have non-zero values.

Optics EXPRESS

$$R = \begin{bmatrix} \mathbf{R}^{\mathrm{TE}\to\mathrm{TE}} & \mathbf{R}^{\mathrm{TM}\to\mathrm{TE}} \\ \mathbf{R}^{\mathrm{TE}\to\mathrm{TM}} & \mathbf{R}^{\mathrm{TM}\to\mathrm{TM}} \end{bmatrix} \tag{4}$$

As illustrated in Fig. 2, the diffraction matrix for a planar interface only has diagonal components, whereas the diffraction matrix for a corrugated interface has off-diagonal components with non-zero values due to the coupling among the diffraction channels and polarization conversion (see Supplement 1, Fig. S1, for the calculated diffraction matrices for actual structures).

The propagation inside the organic material above and below the emission plane can be described by using diagonal matrices $\mathbf{P}_+$ and $\mathbf{P}_-$, respectively. The polarization-independent m-th diagonal element of the propagation matrices is defined as $P^{\mathrm{TE,TM}}_{\pm\, m,m} = e^{ik_{z,m}h_\pm}$, where $k_{z,m} = (n^2_{\mathrm{org}}k_0^2 - (k_x + mG)^2 - k_y^2)^{1/2}$ is the out-of-plane wavevector and h_+ and h_- are the thickness of the organic layer above ($h_+ = h_{\mathrm{org}} - h_{\mathrm{dip}}$) and below ($h_- = h_{\mathrm{dip}} - 1/2 \cdot h_{\mathrm{corr}}$) the emitter, respectively. We note that, to get an accurate result, it is important to take into account evanescent waves with imaginary $k_{z,m}$.

To characterize the light emission from an emitter inside an OLED, two important quantities should be obtained: the total power emitted by the emitter inside the device (F) and the outcoupled light power that eventually escapes the device (F_{out}). Their ratio, F_{out}/F, determines the light extraction efficiency (LEE) for the emitter [42,43]. The total emitted power by an oscillating electric dipole with frequency ω and dipole moment $p_0\hat{\mathbf{p}}$, where $\hat{\mathbf{p}}$ is a unit vector specifying the dipole orientation, can be obtained from the electric field $\mathbf{E}_{\mathrm{emit}}$ at the dipole position $\mathbf{r}_0$ [44],

$$\begin{aligned} F &= -\frac{1}{2}\mathrm{Re}\left\{\int \mathbf{E}(\mathbf{r})\cdot\mathbf{j}^*(\mathbf{r})d^3r\right\} \\ &= \frac{1}{2}\omega p_0\hat{\mathbf{p}}\cdot\mathrm{Im}\{\mathbf{E}_{\mathrm{emit}}(\mathbf{r}_0)\} \\ &= \frac{1}{2}\omega p_0\hat{\mathbf{p}}\cdot\mathrm{Im}\left\{\frac{n^2_{\mathrm{org}}k_0^2}{4\pi^2}\iint_{-\infty}^{\infty}\mathbf{E}_{\mathrm{emit}}(\mathbf{u})e^{i\mathbf{k}\cdot\mathbf{r}_0}du_xdu_y\right\} \\ &= \frac{n^2_{\mathrm{org}}k_0^2}{4\pi^2}\iint_{-\infty}^{\infty}K(\mathbf{u})du_xdu_y, \end{aligned} \tag{5}$$

where $\mathbf{j}$ is the current density associated with the dipole. $K(\mathbf{u})$ determines the emitted power density as a function of in-plane wavevector as follows [44]:

$$K(\mathbf{u}) = \frac{1}{2}\omega p_0\hat{\mathbf{p}}\cdot\mathrm{Im}\{\mathbf{E}_{\mathrm{emit}}(\mathbf{u})\cdot e^{i\mathbf{k}\cdot\mathbf{r}_0}\}. \tag{6}$$

It is important to note that, even with the same dipole moment, the emitted power from a dipole can be significantly different depending on its optical environment; $\mathbf{E}_{\mathrm{emit}}$ is not only affected by the electric field produced by the dipole itself but also depends on the electric field of the additional waves formed by multiple reflections inside the device. Therefore, $\mathbf{E}_{\mathrm{emit}}$ can be written as the sum of three components,

$$\mathbf{E}_{\mathrm{emit}} = \mathbf{E}_0 + \mathbf{E}_{\mathrm{up}} + \mathbf{E}_{\mathrm{down}}, \tag{7}$$

where $\mathbf{E}_0$ is the contribution of the plane waves initially emitted from the dipole and $\mathbf{E}_{\mathrm{up}}$ and $\mathbf{E}_{\mathrm{down}}$ are from the secondary waves propagating upward and downward after reflections. The complex electric amplitude $\mathbf{A}_0$, $\mathbf{A}_{\mathrm{up}}$, and $\mathbf{A}_{\mathrm{down}}$ are obtained by using the following relation (the conversion between the complex amplitude a and the electric field $\mathbf{E}$ are provided in Supplement

Optics EXPRESS

1):

$$\mathbf{A}_0 = \mathbf{X}\mathbf{A}_{\pm} \tag{8}$$

$$\mathbf{A}_{\text{up}} = \mathbf{P}_{-}\mathbf{R}_{-}(\mathbf{I} - \mathbf{C}_{+}\mathbf{C}_{-})^{-1}(\mathbf{P}_{-}\mathbf{X}\mathbf{A}_{-} + \mathbf{C}_{+}\mathbf{P}_{+}\mathbf{X}\mathbf{A}_{+}) \tag{9}$$

$$\mathbf{A}_{\text{down}} = \mathbf{P}_{+}\mathbf{R}_{+}(\mathbf{I} - \mathbf{C}_{-}\mathbf{C}_{+})^{-1}(\mathbf{P}_{+}\mathbf{X}\mathbf{A}_{+} + \mathbf{C}_{-}\mathbf{P}_{-}\mathbf{X}\mathbf{A}_{-}). \tag{10}$$

$\mathbf{A}_+$ and $\mathbf{A}_-$ are the complex amplitudes of the waves emitted upward and downward, respectively, from a dipole with the same dipole moment located at the origin. The values of the decomposed electric amplitude $\mathbf{A}_{\pm}$ are specified in Table 2 [33,45]. $\mathbf{X}$ is a diagonal matrix, $X_{m,m}^{\text{TE,TM}} = e^{-i\mathbf{k}_m \cdot \mathbf{r}_0}$, takes into account the actual position ($\mathbf{r} = \mathbf{r}_0$) of the dipole in Fourier transformation. $\mathbf{R}_+$ and $\mathbf{R}_-$ are the reflection matrices for the top and bottom interface of the organic layer, respectively. $(\mathbf{I} - \mathbf{C}_+\mathbf{C}_-)^{-1}$ accounts for the infinite reflection in the organic layer, where $\mathbf{C}_{\pm} = \mathbf{P}_+\mathbf{P}_-\mathbf{R}_{\pm}$. When the dipole is located in an infinite bulk material with the index n_{org}, only the direct emission term, $\mathbf{A}_0$, survives and the secondary contributions, $\mathbf{A}_{\text{up}}$ and $\mathbf{A}_{\text{down}}$, vanish since there is no reflection. In this case, the total emitted power by the dipole is $F_\infty = n_{\text{org}} c p_0^2 k_0^4/(12\pi\epsilon_0)$. The Purcell factor, η, which describes the enhancement of a spontaneous emission rate, is defined as the ratio of F in the device to F_∞, $\eta = F/F_\infty$ [42].

Table 2. Electric amplitude of a plane wave for different dipole orientations and polarizations.

$a_{\pm}\left(\frac{ip_0k_0}{2n_{\text{org}}\epsilon_0}\right)^{-1}$	TE	TM
x-oriented dipole	$u_y/u_z u_{\parallel}$	$\pm u_x/u_{\parallel}$
y-oriented dipole	$-u_x/u_z u_{\parallel}$	$\pm u_y/u_{\parallel}$
z-oriented dipole	0	$u_{\parallel}/u_z$

The outcoupled light power, F_{out}, can be obtained from the electric amplitude of the waves at the top surface of the organic layer, $\mathbf{A}_{\text{top}}$, which can be obtained from the following relation:

$$\mathbf{A}_{\text{top}} = (\mathbf{I} - \mathbf{C}_{-}\mathbf{C}_{+})^{-1}(\mathbf{P}_{+}\mathbf{X}\mathbf{A}_{+} + \mathbf{C}_{-}\mathbf{P}_{-}\mathbf{X}\mathbf{A}_{-}) \tag{11}$$

The interpretation of this relation is evident: the waves at the top surface consist of the infinite reflections ($(\mathbf{I} - \mathbf{C}_-\mathbf{C}_+)^{-1}$) of (1) the waves that are initially emitted upward from a dipole at $\mathbf{r} = \mathbf{r}_0$ and propagate to the top surface ($\mathbf{P}_+\mathbf{X}\mathbf{A}_+$), (2) the waves that are initially emitted downward, propagate to and reflect from the bottom surface, and then propagate to the top surface ($\mathbf{C}_-\mathbf{P}_-\mathbf{X}\mathbf{A}_- = \mathbf{P}_+\mathbf{P}_-\mathbf{R}_-\mathbf{P}_-\mathbf{X}\mathbf{A}_-$). The outcoupled power density at a given wavevector $\mathbf{u}$ can be obtained from the electric amplitude at the top surface using the following relation [33]:

$$K_{\text{out}}(\mathbf{u}) = \frac{1}{2} n_{\text{org}} c \epsilon_0 |a_{\text{top}}(\mathbf{u})|^2 \text{Re}(u_z) T_+(\mathbf{u}) \tag{12}$$

where $T_+(\mathbf{u})$ is the transmittance of the top surface for the normalized wavevector $\mathbf{u}$ and $\text{Re}(u_z)$ accounts for the vertical energy flow. The net outcoupled light power is obtained by summing up K_{out} over the reciprocal space [33].

$$F_{\text{out}} = \frac{n_{\text{org}}^2 k_0^2}{4\pi^2} \int_{-\infty}^{\infty} \int_{-\infty}^{\infty} K_{\text{out}}(\mathbf{u}) du_x du_y \tag{13}$$

The simulation time and accuracy of the developed DMM method are affected by two factors: the number of Fourier orders considered in RCWA calculation ($-n_{\text{RCWA}} : n_{\text{RCWA}}$) and the reciprocal space resolution (Δk). n_{RCWA} determines the accuracy of the reflection and transmission coefficients calculated in RCWA, since the shape of a periodic corrugation can be represented more accurately in the reciprocal space with more Fourier harmonics. Δk

Optics EXPRESS

determines the distance between two nearest sampling points in the reciprocal space, and the number of sampling points in the Brillouin zone is given by $n_{BZ} = G/\Delta k$. As n_{BZ} increases, the numerical integration of LEE and Purcell factor becomes more accurate. The computation time is roughly proportional to the square of n_{RCWA} and n_{BZ} for devices with one-dimensional periodic corrugation (see Supplement 1 for more details). In most cases, the size of the diffraction matrix ($N = 2M + 1$) has a lower impact on the accuracy of the calculation compared to n_{RCWA} or n_{BZ} as long as N is large enough to cover surface plasmons at metal-dielectric interfaces since the power fraction of the dipole emission becomes almost negligible beyond that point. Here, we set N to cover $|u_{\parallel}| \leq 2.5$ in the reciprocal space.

3. Results and discussion

The DMM developed in this work is demonstrated using a simplified OLED structure at a fixed emission wavelength of $\lambda_0 = 520$ nm throughout the article, assuming a green phosphorescent light. As shown in Fig. 3(a), the structure consists of three layers: a periodically corrugated semi-infinite Al electrode with the period $P = 340$ nm and the peak-to-peak corrugation amplitude $h_{corr} = 20$ nm, an organic layer with the refractive index $n_{org} = 1.8$ and the height $h_{org} = 225$ nm, and a thin Ag electrode of the thickness $h_{Ag} = 15$ nm. The complex permittivities of the Al and Ag electrodes at $\lambda_0 = 520$ nm are taken from Palik et al. [46]. The corrugation is set to have a square profile with 50% duty cycle. The emission layer of the device is located $h_{dip} = 65$ nm above the center of the corrugation.

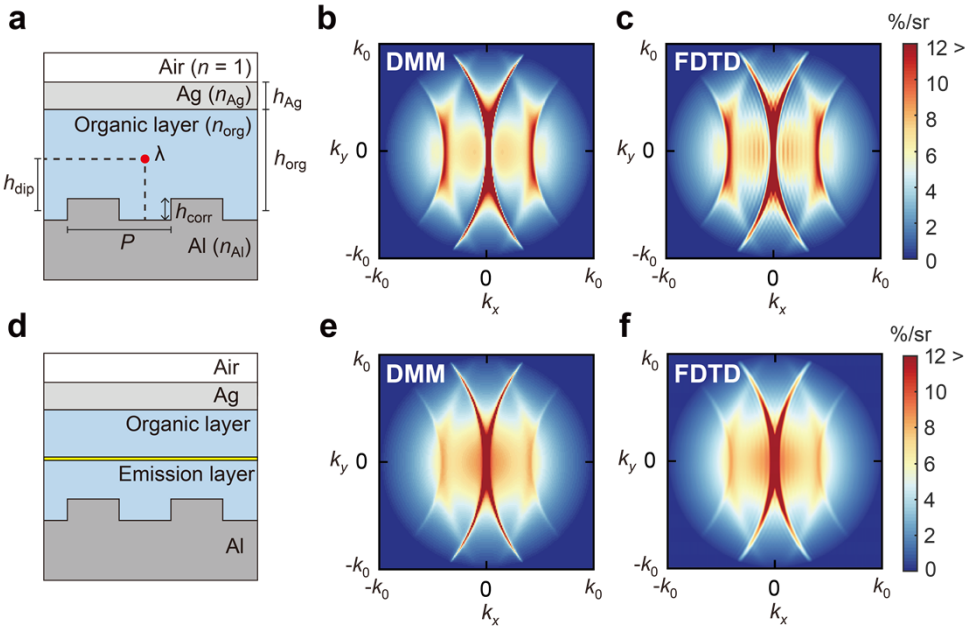

Fig. 3. Far-field computation results of DMM. (a) A simplified schematic of a corrugated OLED with a point emission source. **(b)** and **(c)** show the far-field intensity of the corrugated OLED with a point source simulated by DMM and FDTD, respectively. Both images show the same far-field intensity pattern, ignoring the ripples in the FDTD simulation result. **(d)** A simplified schematic of a corrugated OLED with planar inhomogeneous emission. The structure parameters are the same as described in **(a)**. Subfigures **(e)** and **(f)** show the calculated far-field intensity of the corrugated OLED with planar inhomogeneous source analytically integrated by DMM and the average of multiple dipole positions simulated by FDTD, respectively.

Optics EXPRESS

We first compare DMM with the conventional FDTD method for a single emitter illustrated in Fig. 3(a). The emitter is assumed to be isotropic, whose optical properties can be obtained by averaging the optical responses of x, y, and z-oriented dipoles. The horizontal position of the single emitter is the center of the two neighboring metallic grating. The converged value of the overall LEE (and Purcell factor) obtained by using DMM and FDTD are 15.89% (1.268) and 15.96% (1.243), respectively, confirming that the two methods quantitatively agree within 2% (see Section S4 of Supplement 1 for detailed results). The extracted light from an OLED can be decomposed according to its wavevector or direction of propagation. The far-field emission patterns of the model device calculated using DMM and FDTD are displayed in Fig. 3(b) and 3(c), respectively, which also show good agreement with the diffraction arcs and the emission peaks appearing at the same position in the reciprocal space. However, a high-frequency ripple-like feature is observed only in the FDTD result (Fig. 3(c)) due to the finite simulation space, as shown in Figure S4. On the other hand, the result from DMM does not suffer from such an artifact since DMM intrinsically deals with an infinite real-space by formulating problem in the reciprocal space.

To evaluate the overall light emission properties of an OLED device, it is necessary to integrate the responses of numerous incoherent emitters in the emission plane, as depicted in Fig. 3(d). Since both the orientation of a dipole and its position relative to the corrugation affect the emission properties of the dipole [26,47], the conventional way to solve this problem is to run multiple single-dipole simulations with various dipole orientations and positions, and average the resulting responses. For our example device with one-dimensional corrugation, more than 12 simulations (4 positions $\times$ 3 orientations each) are required to ensure convergence (see Section S6 of Supplement 1 for a detailed analysis).

Unlike conventional methods, DMM can accurately calculate the averaged emission properties of an emission plane at the same computational cost as a single dipole simulation. Since the diffraction matrices are unaffected by dipole orientation, and the information of the dipole position $\mathbf{r}_0$ is encoded only in $\mathbf{X}$, it is possible to analytically perform integration over the dipole position and orientation without the effort of running multiple simulations (see Section S7 of Supplement 1 for mathematical formulation). As shown in Fig. 3(e) and 3(f), the calculated far-field intensity patterns from an emission plane using DMM and FDTD (averaged over 7 dipole positions and 3 dipole orientations) match with a 1.19% difference in LEE. The overall LEE of the corrugated OLED is estimated to be 14.49%, which is a 26% enhancement compared to the flat device with the same layer thicknesses.

We then compared the simulation speed of DMM and FDTD for various light emission problems. Here, we used a server computer equipped with two Intel Xeon Gold 5220 CPUs @ 2.20 GHz and 256GB of RAM for both simulation methods. In order to make a fair comparison between the methods, we chose the parameters of each calculation method - n_{RCWA}, Δk, and N for DMM, and the mesh size and the simulation volume for FDTD - as they minimize the calculation time while ensuring convergence within 1% of ground truth value based on Section S8 of Supplement 1. As summarized in Fig. 4(a), for the point emitter presented in Fig. 3(a)-(c), DMM (185 s) is about 60 times faster than FDTD (11,200 s). For the planar emission shown in Fig. 3(d)-(f), DMM achieves an additional speedup factor of twelve accounting for various dipole positions and orientations, making it 780 times faster than FDTD.

It is important to note that DMM can be much more efficient in case the diffraction matrices can be reused, since the determination of the diffraction coefficients using RCWA consumes 95% of the computation time (see Section S9 of Supplement 1 for detailed process flow). As the diffraction coefficients are only dependent on the structural parameters for the periodic corrugation, changing other parameters, such as dipole position, dipole orientation, and the thicknesses of the composing layers, leaves the diffraction matrices unchanged. Consequently, DMM has a strong advantage at performing optimizations or parametric sweeps, or even applying

Optics EXPRESS

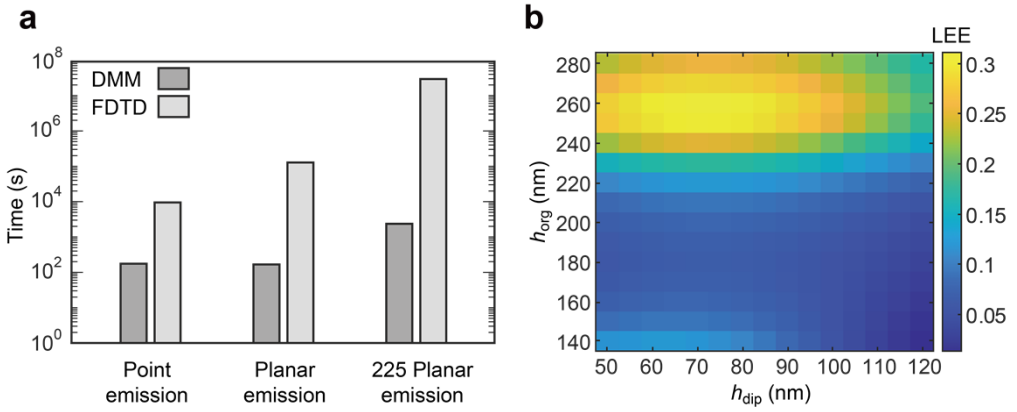

Fig. 4. Speedup in structure optimization using DMM. (a) Histogram comparing the computational time of DMM and FDTD for calculating the LEE of a single dipole emission, planar inhomogeneous emission, and planar inhomogeneous emission in 225 different conditions (varying organic layer thicknesses and dipole heights). The histogram shows that DMM is faster than FDTD for all cases. **(b)** LEE distribution for 15 different organic layer thicknesses (ranging from 140 nm to 280 nm with 10 nm increments) and 15 different dipole heights (ranging from 50 nm to 120 nm with 5 nm increments) for the structure shown in Fig. 3. The diffraction matrices can be reused because the corrugation structure parameters remain unchanged.

machine learning techniques to these parameters by methods, as are done for planar OLEDs [28,48]. As an example, the LEE calculation of planar emission in a corrugated OLED with 225 different combinations of h_{dip} and h_{org} using DMM is shown in Fig. 4(b). We could easily find the optimal parameters h_{dip} and h_{org}. Since the diffraction matrices are reused after the initial calculation, the measured additional time required to simulate a different structure is only 5%. The optimized parameters are slightly different as h_{corr} increases (see Section S10 of Supplement 1 for detailed information). The overall calculation time of 225 different OLED devices using DMM is 2536 s, which is over 10^4 times faster than FDTD and even shorter than the time of a single FDTD simulation, as shown in Fig. 4(a). As a final remark, we note that DMM discretizes the light emission problem in the reciprocal space and thus it is possible to significantly reduce the simulation time in case one needs the light emission properties at a small set of in-plane wavevectors or emission angles.

DMM is not only faster than conventional full-wave simulation methods but is also advantageous in quantitative mode analyses. Since DMM is formulated in reciprocal space, it naturally enables a quantitative analysis of power dissipation channels of the device according to their wavevectors. Figure 5(a) and 5(b) compare the reciprocal space distribution of the power dissipation density, $K(\mathbf{u})$, in planar and corrugated OLED devices. In the device without corrugation, $K(\mathbf{u})$ is distributed isotropically, exhibiting a few concentric rings associated with the characteristic eigenmodes residing in the device. As seen in Fig. 5(c), obtained by azimuthal integration of Fig. 5(a) and 5(b), a large fraction of power is dissipated into three distinct modes peaked at u = 0.61, 0.85, and 1.02, of which the former two are the fundamental and second-order waveguide modes (WG1, WG2) and the latter is the surface plasmon polariton mode (SPP) at the interface between the organic layer and the bottom electrode. When x-directional periodic corrugation with Δu = 0.85 is applied, strong diffraction arcs appear, and two WG2 modes are diffracted to the Γ point by 1st and -1st diffraction, overlapping each other as shown in Fig. 5(b). Due to mode conversion from the WG2 mode, normal directional outcoupled power in the corrugated device is enhanced by more than threefold compared to the planar device, as seen in the angular

Optics EXPRESS

emission pattern in Fig. 5(d). WG1 mode and SPP mode can also be diffracted into the light cone and achieve some chance to escape the device with non-zero in-plane wavevectors as seen in Fig. 5(b). As a result, the corrugated device emits better than its planar counterpart even at off-normal angles (Fig. 5(d)).

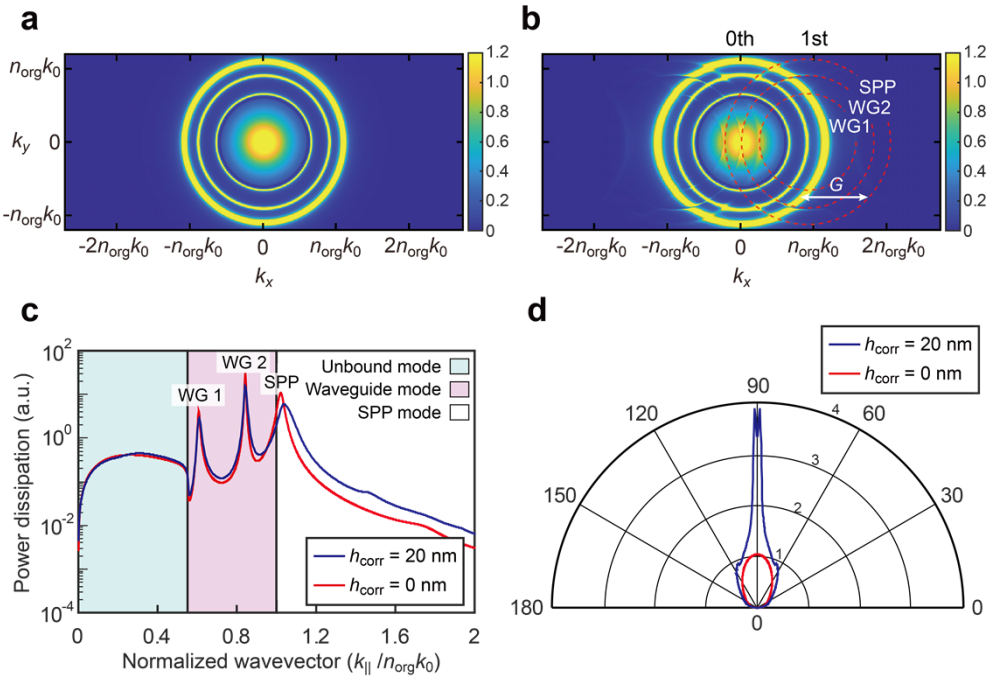

Fig. 5. Power dissipation mode analysis. (a), (b) Power dissipation density pattern for **(a)** a planar OLED and **(b)** a corrugated OLED (h_{corr} = 20 nm). The corrugation induces diffraction which leads to the shift of dissipation density pattern by the crystal momentum (G). **(c)** Circular integration of power dissipation density pattern. High power dissipation peaks in the SPP mode is broadened. **(d)** Angular dependence of outcoupled power of planar and corrugated OLED. Outcoupled power of corrugated OLED outperforms that of planar OLED, especially in normal direction. The values in **(a), (b)** are normalized so that the integration of the color plot leads to the Purcell factor.

The presented method can be readily extended to devices with two-dimensional corrugation. An OLED device with a two-dimensional corrugation is considered as shown in Fig. 6(a). It shares the same structural parameters as 1D corrugation, and for simplicity, we assume the corrugation to be a square grating with P_x = 340 nm, P_y = 340 nm. The horizontal position of the single emitter is at the center of the four metallic slabs which form a square. In this case, the in-plane wavevectors of the diffracted waves also form a square lattice in reciprocal space as shown in Fig. 6(b). The trivial representation of the diffraction coefficients for a two-dimensional corrugation would be a rank 2 matrix, but in order to use the identical formalism used for one-dimensional corrugation, we flatten the matrix representing the diffraction coefficient into a column vector. As the diffracted waves from a single plane wave are represented by a vector as in 1D corrugation, implementation of DMM for a 2D corrugated OLED can be done without further complication (see Section S11 of Supplement 1 for the detailed description of the method). As shown in Fig. 6(c), the resulting power dissipation density shows the distinctive diffraction arcs associated with the crystal momentum and the C4 symmetry of the square corrugation. Due to the power conversion from the second-order waveguide mode to the outcoupled modes, the

Optics EXPRESS

overall LEE of the device is enhanced by 44.5% and 17.1% compared to the flat device and the 1D corrugated device with the same periodicity, respectively.

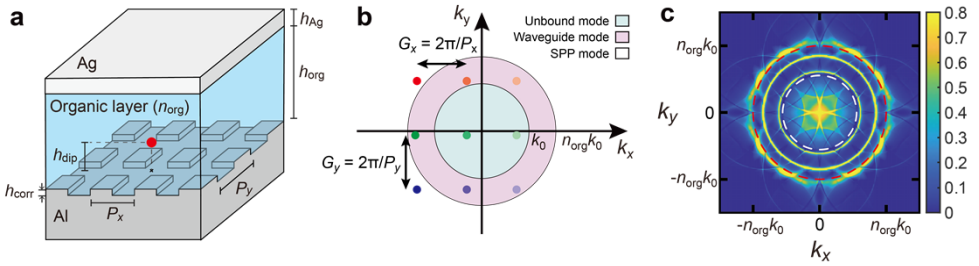

Fig. 6. DMM method for OLED with 2D corrugation. **(a)** A simplified schematic 2D corrugated OLED with the point emission source. **(b)** In-plane wavevectors of the diffracted planewaves are represented as dots in the reciprocal space. The distance between the two neighboring dots is equal to $G_x = 2\pi/P_x$ or $G_y = 2\pi/P_y$. **(c)** Power dissipation pattern of a 2D corrugated OLED calculated by DMM. The white and red concentric rings represent the boundaries between the unbound and the waveguide, the waveguide and the SPP mode, respectively.

4. Conclusion

In this work, we have developed a computational method, DMM, that enables the calculation of the dipole emission and its outcoupling in a periodically corrugated OLED device. The effectiveness of DMM was examined by making a direct comparison with FDTD. The LEE and Purcell factor calculation results using DMM and FDTD agrees within an error smaller than 2%, while DMM runs ~60 times faster. DMM achieved $\sim 10^4$ speedup for performing optimizations of grating-unrelated parameters by reusing the diffraction matrices. Additionally, DMM is capable of conducting power dissipation analysis, which is impossible in FDTD. Power dissipation analysis resolves power dissipation channels into an unbound mode, a waveguide mode, and an SPP mode. Such analysis helps identify energy loss channels. We successfully extended DMM to OLEDs with 2D corrugation and demonstrated good agreement with FDTD results within a 3% error. Code 1 for DMM is available on GitHub [49], and further development will be pursued.

It should be noted that DMM provides accurate solutions only for devices with perfect periodic corrugations, since it reduces the complexity of electromagnetic simulations by using discrete bases defined by the crystal momentum. However, we anticipate that DMM, with some modification, could also handle problems with a non-perfect or quasi periodicity by decomposing the problem into a linear combination of periodic devices with different periodicities and orientations.

We envision that DMM would enable the search for an optimal corrugated LED structure that provides higher LEE than that of an optimal planar device. Moreover, DMM can be utilized for characterizing the optical properties of any photonic device that involves a wide-angle incidence within periodic geometry such as perovskite LEDs and quantum dot (QD) displays.

Funding. LG Display; Ministry of Trade, Industry and Energy (1415180303); Korea Semiconductor Research Consortium (20019357); National Research Foundation of Korea (BK21 FOUR Program); Ministry of Science and ICT, South Korea (NRF-2017R1A5A1014708).

Disclosures. The authors declare no conflicts of interest.

Data availability. Data underlying the results presented in this paper are not publicly available at this time but may be obtained from the authors upon reasonable request. Code 1 for DMM is available on GitHub [49].

Optics EXPRESS

Supplemental document. See Supplement 1 for supporting content.

References

1. T. Sekitani, H. Nakajima, H. Maeda, T. Fukushima, T. Aida, K. Hata, and T. Someya, "Stretchable active-matrix organic light-emitting diode display using printable elastic conductors," Nat. Mater. **8**(6), 494–499 (2009).
2. M.S. White, M. Kaltenbrunner, E.D. Glowacki, K. Gutnichenko, G. Kettlgruber, I. Graz, S. Aazou, C. Ulbricht, D.A.M. Egbe, M.C. Miron, Z. Major, M.C. Scharber, T. Sekitani, T. Someya, S. Bauer, and N.S. Sariciftci, "Ultrathin, highly flexible and stretchable PLEDs," Nat. Photonics **7**(10), 811–816 (2013).
3. F. So, J. Kido, and P. Burrows, "Organic light-emitting devices for solid-state lighting," MRS Bull. **33**(7), 663–669 (2008).
4. H.W. Chen, J.H. Lee, B.Y. Lin, S. Chen, and S.T. Wu, "Liquid crystal display and organic light-emitting diode display: present status and future perspectives," Light: Sci. Appl. **7**(1), 1 (2018).
5. Y.G. Huang, E.L. Hsiang, M.Y. Deng, and S.T. Wu, "Mini-LED, Micro-LED and OLED displays: present status and future perspectives," Light: Sci. Appl. **9**(1), 105 (2020).
6. H.P. Zhao, G.Y. Liu, J. Zhang, R.A. Arif, and N. Tansu, "Analysis of internal quantum efficiency and current injection efficiency in III-nitride light-emitting diodes," J. Disp. Technol. **9**(4), 212–225 (2013).
7. A. Salehi, X.Y. Fu, D.H. Shin, and F. So, "Recent Advances in OLED Optical Design," Adv. Funct. Mater. **29**(15), 1808803 (2019).
8. J. Song, H. Lee, E.G. Jeong, K.C. Choi, and S. Yoo, "Organic light-emitting diodes: pushing toward the limits and beyond," Adv. Mater. **32**(35), 1907539 (2020).
9. Y. Qu, J. Kim, C. Coburn, and S.R. Forrest, "Efficient, nonintrusive outcoupling in organic light emitting devices using embedded microlens arrays," ACS Photonics **5**(6), 2453–2458 (2018).
10. M. Thomschke, S. Reineke, B. Lussem, and K. Leo, "Highly efficient white top-emitting organic light-emitting diodes comprising laminated microlens films," Nano Lett. **12**(1), 424–428 (2012).
11. J.B. Kim, J.H. Lee, C.K. Moon, S.Y. Kim, and J.J. Kim, "Highly Enhanced Light Extraction from Surface Plasmonic Loss Minimized Organic Light-Emitting Diodes," Adv. Mater. **25**(26), 3571–3577 (2013).
12. H.W. Chang, J. Lee, S. Hofmann, Y.H. Kim, L. Muller-Meskamp, B. Lussem, C.C. Wu, K. Leo, and M.C. Gather, "Nano-particle based scattering layers for optical efficiency enhancement of organic light-emitting diodes and organic solar cells," J. Appl. Phys. **113**(20), 204502 (2013).
13. K.Y. Yang, K.C. Choi, and C.W. Ahn, "Surface plasmon-enhanced spontaneous emission rate in an organic light-emitting device structure: Cathode structure for plasmonic application," Appl. Phys. Lett. **94**(17), 173301 (2009).
14. J. Song, K.H. Kim, E. Kim, C.K. Moon, Y.H. Kim, J.J. Kim, and S. Yoo, "Lensfree OLEDs with over 50% external quantum efficiency via external scattering and horizontally oriented emitters," Nat. Commun. **9**(1), 3207 (2018).
15. S. Jeon, S. Lee, K.H. Han, H. Shin, K.H. Kim, J.H. Jeong, and J.J. Kim, "High-quality white OLEDs with comparable efficiencies to LEDs," Adv. Opt. Mater. **6**(8), 1701349 (2018).
16. Y. Qu, C. Coburn, D.J. Fan, and S.R. Forrest, "Elimination of plasmon losses and enhanced light extraction of top-emitting organic light-emitting devices using a reflective subelectrode grid," ACS Photonics **4**(2), 363–368 (2017).
17. Y., Sun and S.R. Forrest, "Enhanced light out-coupling of organic light-emitting devices using embedded low-index grids," Nat. Photonics **2**(8), 483–487 (2008).
18. J. Frischeisen, Q.A. Niu, A. Abdellah, J.B. Kinzel, R. Gehlhaar, G. Scarpa, C. Adachi, P. Lugli, and W. Brutting, "Light extraction from surface plasmons and waveguide modes in an organic light-emitting layer by nanoimprinted gratings," Opt. Express **19**(S1), A7–A19 (2011).
19. W. Youn, J. Lee, M.F. Xu, R. Singh, and F. So, "Corrugated Sapphire Substrates for Organic Light-Emitting Diode Light Extraction," ACS Appl. Mater. Interfaces **7**(17), 8974–8978 (2015).
20. W.H. Koo, S.M. Jeong, F. Araoka, K. Ishikawa, S. Nishimura, T. Toyooka, and H. Takezoe, "Light extraction from organic light-emitting diodes enhanced by spontaneously formed buckles," Nat. Photonics **4**(4), 222–226 (2010).
21. C. Fuchs, P.A. Will, M. Wieczorek, M.C. Gather, S. Hofmann, S. Reineke, K. Leo, and R. Scholz, "Enhanced light emission from top-emitting organic light-emitting diodes by optimizing surface plasmon polariton losses," Phys. Rev. B **92**(24), 245306 (2015).
22. A. Chutinan, K. Ishihara, T. Asano, M. Fujita, and S. Noda, "Theoretical analysis on light-extraction efficiency of organic light-emitting diodes using FDTD and mode-expansion methods," Org. Electron. **6**(1), 3–9 (2005).
23. A.O. Altun, S. Jeon, J. Shim, J.H. Jeong, D.G. Choi, K.D. Kim, J.H. Choi, S.W. Lee, E.S. Lee, H.D. Park, J.R. Youn, J.J. Kim, Y.H. Lee, and J.W. Kang, "Corrugated organic light emitting diodes for enhanced light extraction," Org. Electron. **11**(5), 711–716 (2010).
24. Y. Qu, M. Slootsky, and S.R. Forrest, "Enhanced light extraction from organic light-emitting devices using a sub-anode grid," Nat. Photonics **9**(11), 758–763 (2015).
25. Y.G. Li, M. Kovacic, J. Westphalen, S. Oswald, Z.F. May, C. Hanisch, P.A. Will, L.H. Jiang, M. Junghaehnel, R. Scholz, S. Lenk, and S. Reineke, "Tailor-made nanostructures bridging chaos and order for highly efficient white organic light-emitting diodes," Nat. Commun. **10**(1), 1 (2019).
26. H., Luder and M. Gerken, "FDTD modelling of nanostructured OLEDs: analysis of simulation parameters for accurate radiation patterns," Opt. Quantum Electron. **51**(5), 139 (2019).

Optics EXPRESS

27. R. Chance, A. Prock, and R. Silbey, "Molecular fluorescence and energy transfer near interfaces," Adv. Chem. Phys. **37**, 1–65 (1978).
28. S. Kim, J.M. Shin, J. Lee, C. Park, S. Lee, J. Park, D. Seo, S. Park, C.Y. Park, and M.S. Jang, "Inverse design of organic light-emitting diode structure based on deep neural networks," Nanophotonics **10**(18), 4533–4541 (2021).
29. J. Park, S. Kim, D.W. Nam, H. Chung, C.Y. Park, and M.S. Jang, "Free-form optimization of nanophotonic devices: from classical methods to deep learning," Nanophotonics **11**(9), 1809–1845 (2022).
30. Y., Zhang and R. Biswas, "High Light Outcoupling Efficiency from Periodically Corrugated OLEDs," ACS Omega **6**(13), 9291–9301 (2021).
31. H. Rigneault, F. Lemarchand, and A. Sentenac, "Dipole radiation into grating structures," J. Opt. Soc. Am. A **17**(6), 1048–1058 (2000).
32. K. Postava, T. Fordos, H. Jaffres, L. Halagacka, H.J. Drouhin, and J. Pistora, "Modeling of anisotropic grating structures with active dipole layers," Integrated Optics: Physics and Simulations Ii **9516**, 95160O (2015).
33. D. Delbeke, P. Bienstman, R. Bockstaele, and R. Baets, "Rigorous electromagnetic analysis of dipole emission in periodically corrugated layers: the grating-assisted resonant-cavity light-emitting diode," J. Opt. Soc. Am. A **19**(5), 871–880 (2002).
34. M.K. Callens, H. Marsman, L. Penninck, P. Peeters, H. de Groot, J.M. ter Meulen, and K. Neyts, "RCWA and FDTD modeling of light emission from internally structured OLEDs," Opt. Express **22**(S3), A589–A600 (2014).
35. C. Wiesmann, Nano-structured LEDs–Light extraction mechanisms and applications. Dissertation, Univeristät Regensburg, 2010.
36. V., Liu and S. Fan, "S4: A free electromagnetic solver for layered periodic structures," Comput. Phys. Commun. **183**(10), 2233–2244 (2012).
37. U. Rau, "Reciprocity relation between photovoltaic quantum efficiency and electroluminescent emission of solar cells," Phys. Rev. B **76**(8), 085303 (2007).
38. J.J. Greffet, P. Bouchon, G. Brucoli, and F. Marquier, "Light Emission by Nonequilibrium Bodies: Local Kirchhoff Law," Phys. Rev. X **8**(2), 021008 (2018).
39. C.W., Tang and S.A. Vanslyke, "Organic electroluminescent diodes," Appl. Phys. Lett. **51**(12), 913–915 (1987).
40. J.P., Hugonin and P. Lalanne, "Reticolo software for grating analysis," arXiv, arXiv:2101.00901, (2021).
41. L. Li, "A modal-analysis of lamellar diffraction gratings in conical mountings," J. Mod. Opt. **40**(4), 553–573 (1993).
42. M. Furno, R. Meerheim, S. Hofmann, B. Lussem, and K. Leo, "Efficiency and rate of spontaneous emission in organic electroluminescent devices," Phys. Rev. B **85**(11), 115205 (2012).
43. A., Egel and U. Lemmer, "Dipole emission in stratified media with multiple spherical scatterers: Enhanced outcoupling from OLEDs," J. Quant. Spectrosc. Radiat. Transfer **148**, 165–176 (2014).
44. K.T. McDonald, *Decomposition of Electromagnetic Fields into Electromagnetic Plane Waves*. (Princeton University, Princeton, 2010).
45. K.G., Sullivan and D.G. Hall, "Enhancement and inhibition of electromagnetic radiation in plane-layered media .1. Plane-wave spectrum approach," J. Opt. Soc. Am. B **14**(5), 1149–1159 (1997).
46. E.D. Palik, *Handbook of optical constants of solids*, Vol. 3. (Academic, 1998).
47. M. Kovacic, "Effect of dipole position and orientation on light extraction for red OLEDs on periodically corrugated substrate - FEM simulations study," Informacije Midem-Journal of Microelectronics Electronic Components and Materials **51**(1), 73–84 (2021).
48. G.J. Tan, J.H. Lee, S.C. Lin, R.D. Zhu, S.H. Choi, and S.T. Wu, "Analysis and optimization on the angular color shift of RGB OLED displays," Opt. Express **25**(26), 33629–33642 (2017).
49. C. Park, J. Shin, and M. S. Jang, "DMM: Diffraction Matrix Method, github, (2023), https://github.com/jLabKAIST/DiffractionMatrixMethod_DMM.